Soft Matter

Dislocation mechanisms in the plastic deformation of monodisperse wet foams within an expansion-contraction microfluidic geometry

Journal:	*Soft Matter*
Manuscript ID	SM-ART-03-2019-000477.R1
Article Type:	Paper
Date Submitted by the Author:	05-Jun-2019
Complete List of Authors:	Vecchiolla, Daniel; Rice University, Chemical & Biomolecular Engineering Biswal, Sibani; Rice University, Chemical & Biomolecular Engineering

Dislocation mechanisms in the plastic deformation of monodisperse wet foams within an expansion-contraction microfluidic geometry†

Daniel Vecchiolla and Sibani Lisa Biswal*

Densely packed wet foam was subjected to gradual expansion and contraction in a wide (1400-1800 μm) microfluidic channel to study localized plastic deformation events within the monodisperse bubble matrix. Dislocation glide, reflection, nucleation, and dipole transformations from extensional and compressive stresses were observed across a range of fluid flow rates and bubble packing densities. Disparate, cyclic reflections occur in two independent regions of the flowing foam, and the mechanisms of dislocation reflection under tension are expanded. The use of an asymmetric channel created a dichotomy in the model crystalline system between straighter, aligned bubble rows and curved, misaligned rows due to the corresponding streamlines within the channel. The resulting gradient in crystalline alignment had numerous effects on dislocation mobility and plastic deformation. 7/7 dipoles were found to rearrange to a more stable configuration aligned with the foam flow before disassociating. Dislocations comprising 5/5 dipoles (resembling the Inverse-Stone-Wales defect in carbon nanostructures) were discovered to pass through one another *via* intermediate ring structures, which most commonly consisted of three dislocation pairs around a triangular-shaped central bubble.

1 Introduction

The groundbreaking work of Bragg and Nye in the 1940s on soap bubble rafts as 2-D analogs of metal crystals and the formation of 3-D crystalline structures from multiple bubble layers[1] has received renewed interest[2-6] over the last few decades. Microfluidics has enabled rapid generation of stable, ordered monodisperse foams with the simple tuning parameters of the fluid flow rates and the geometrical dimensions of the device. In fact, the study of crystals has been closely coupled with microfluidic foam research from its inception almost twenty years ago. Gañán-Calvo and Gordillo noted the ease of formation of "mesocrystal foam" on a liquid surface[7] upon their rediscovery of flow-focusing[8] bubble production. The role of flow and confinement in two-dimensional microfluidic channels has been studied for colloidal crystals,[9] metastable periodic lattice structures of foam,[10] and tunable bubble lattice diffraction gratings.[11] Flow-focusing has facilitated 3-D crystalline foam structure analysis[12] as well as the construction of highly structured porous solids from foam templates.[13]

However, the utilization of foams (and emulsions) as crystalline systems for studying plastic deformation has largely occurred outside of the microfluidic domain. Rosa and Fortes subjected monodisperse foam confined between surfactant solution and a glass plate (liquid-plate configuration) to tension and compression.[14] Plastic deformation *via* dislocation glide at 60° angles from the wall was observed at the elastic limit. The researchers determined that dislocations reflected at the walls with different mechanisms depending on the direction of the stress, expanding on previous work with soap bubble rafts.[15] Subjecting the foam to tension by means of increasing

Department of Chemical and Biomolecular Engineering, Rice University, Houston, TX 77005, USA. E-mail: biswal@rice.edu; Fax: +1 7133485478

† Electronic supplementary information (ESI) available.

wall separation causes the number of close-packed rows of bubbles parallel to the walls to increase until a neck (i.e. thin film) forms between the two halves.[14] Similarly, pulling apart the confining walls of monodisperse and polydisperse bubbles rafts at constant velocity has shown a competition between two failure modes for foam under tension: plastic pinch-off at low deformation rates and brittle fracture for high deformation rates.[16,17] Dislocation nucleation from nanoindentation was also examined using a bubble raft as a model fcc crystal.[18,19]

A Hele-Shaw cell was employed to determine that the kinematics of flowing, dry foam in a convergent channel are unchanged by the presence of plastic deformation events.[20] Furthermore, the rate of plastic events (i.e. T1 topological rearrangements, see Section 3.2) is proportional to the deformation rate given by the simple velocity field as long as wall friction is negligible. The flow of dense, polydisperse emulsions (area fractions greater than 0.90) in a thin chamber with a constricting hopper shape has demonstrated that localized plastic events reduce and redistribute stress.[21,22] The resulting decrease in the inter-droplet forces lessens the deformation of nearby droplets as far as three diameters away. The quasistatic pipe flow of wet foams was investigated using a modified Surface Evolver simulation and plastic events were found to occur primarily near the wall,[23] as previously evidenced in the liquid-plate configuration.[24] However, the localized shear band was found to widen with increasing gas fraction from 0.88 to 0.94 in polydisperse foams.23,[25] Most recently, dislocation dynamics in a microfluidic crystal comprised of a concentrated, monodisperse emulsion were shown to be highly ordered with applications to flow control systems and the manufacture of nanocrystalline materials.[26]

The plastic deformation of foam has garnered significant attention for applications in materials science as dislocation dynamics play an important role across crystalline fields. In rotating crystals made from magnetic Janus colloids, stress was discovered to spontaneously release by regular repetition of dislocations gliding from the edge to the center when the crystals are larger than a critical size.[27] In spherical crystals, dislocations weakly bound to scars (finite-length high angle grain boundaries[3,28,29]) had a moderately larger diffusion constant than the coefficient for single particles.[30] Dislocation glide and reactions in a 2-D crystal of charged colloids were studied using an array of weak optical tweezers.[31] The nucleation and glide separation of dislocation pairs in tubular crystals (e.g. carbon nanotubes) enables the low energy release of externally applied strain.[32] Dislocation pairs (comprising a dislocation dipole) were found to separate in reduced graphene oxide sheets due to sufficient strain,[33] rather than anneal as detected in crystalline graphene.[34] The formation of stable dislocation pairs developing from large vacancy defect clusters in irradiated graphene was assessed to better understand these processes in three dimensional materials.[35]

The decade-long surge of research in graphene[36,37] and related single sheet materials[38] furthers the renewed demand for studying 2-D crystalline phenomena. Recent foam tension studies have investigated the resulting failure mode,[16,17] rather than the ordered dislocation glide and reflection discovered in the liquid-plate configuration.[14] Confining foam flow between parallel boundaries often limits the majority of the plastic events to the regions near the walls.[23-25] Emulsion experiments in a constricting channel demonstrated the clustering of plastic events,[21,22] but not to the degree of order discovered in a recent monodisperse emulsion study in a tapered microfluidic channel.[26] In the present work, a wider range of dislocation mechanisms is examined by subjecting flowing, monodisperse foam to *extensional* and compressive stresses within an expansion-contraction microfluidic geometry (1400-1800 μm wide). The channel consisted of one horizontal wall and one sinusoidal wall, and the resulting gradient in crystalline alignment had numerous effects on dislocation mobility and plastic deformation.

Section 3.1 introduces the experimental flow and foam parameters that support the formation of microfluidic crystalline lattices. The specific experimental conditions for the model system used to demonstrate the majority of the observed crystalline phenomena is also defined in the context of the recent microfluidic work on flowing, monodisperse emulsions.[26] Section 3.2 provides a condensed background regarding the link between dislocation theory and T1 topological rearrangements that is fundamental to the dislocation glide discussed in Section 3.3. Section 3.4 describes the various dislocation reflection mechanisms observed in tension, expanding on the previous work of Rosa and Fortes.[14] Section 3.5 briefly details the previously established form of dislocation reflection in compression at a physical wall.[14,26] Section 3.6 explains the presence of homogeneous dislocation nucleation in isolated regions of the channel. Lastly, Section 3.7 connects the temporal evolution of dislocation dipoles within the crystalline foam to the analogous defects commonly studied in graphene.

2 Materials and methods

2.1 Design and fabrication

The microfluidic device was fabricated using standard soft lithography methods.[39] Briefly, the microfluidic pattern was created with AutoCAD and transferred onto a 4" silicon wafer by maskless photolithography *via* the SF-100 (Intelligent Micro Patterning LLC now known as Advanced Micro Patterning LLC). The wafer had been spin-coated with SU-8 50 photoresist to a thickness of 50 μm. Monodisperse bubbles were generated using a flow-focusing geometry adapted from a prior design in our lab.[40] The flow-focusing orifice is 20-25 μm wide and the connected narrow channel is 60 μm wide.

5000 μm downstream of the flow-focusing orifice, the narrow channel expands with 45° walls to a width of 1600 μm as in our prior work on bubble-bubble pinch-off in a symmetric expansion.[41] Following the expansion, the 10 000 μm long channel consists of one horizontal wall and one sinusoidal wall. The parameters of the sinusoidal wall are a vertical shift of 1600 μm, an amplitude of 200 μm, and a period of 4000 μm. Therefore, the channel consisted of three valleys (1800 μm wide) and two peaks (1400 μm wide). The period of the sinusoidal wall was optimized to observe the central valley from slightly farther than peak to peak (see Fig. 1a). The utilization of a sinusoidal wall enables gradual (rather than sudden or abrupt[42-46]) expansion and contraction to preserve the crystalline structure of the densely packed wet foam.

The devices were fabricated from PDMS (Slygard 184 silicone elastomer) using a 5:1 base to curing agent ratio for improved stability against wide (>1000 μm) channel collapse as the elastic modulus is roughly 1.6 times greater than conventionally used 10:1 PDMS.[47] PDMS was cured 16-20 hours (90 minutes has since been determined sufficient) on the master pattern at 80°C. The designs were bonded to a microscope slide using oxygen plasma for 20 seconds. DI water was manually flushed through devices within 20 minutes of bonding. Bubble generation was achieved by supplying surfactant solution and air to independent inlets.

2.2 Experimental procedure

1% alpha olefin sulfonate (AOS) 14-16 surfactant solution was injected by a syringe pump (Harvard Apparatus PHD 2000) and air was supplied using a microfluidic pressure pump (Fluigent MFCS-8C). The device was visualized on an inverted microscope (Olympus IX71) at 4x magnification. The foam flow was recorded by a high-speed camera (Phantom V4.3) at 400 fps for conditions at or below 1 mL h^{-1} and 800 fps above 1 mL h^{-1}.

There are two effects to increasing the gas pressure at a constant surfactant solution flow rate: the volume of each bubble increases and fraction of gas in the channel increases.[11] Starting at a low surfactant solution flow rate (e.g. 0.3 mL h^{-1}), the pressure of the gas was increased until the gas area fraction $\Phi > \sim 0.90$ in order for crystalline deformation to occur. Steady state recordings were taken at 25 or 50 mbar pressure intervals. The surfactant solution flow rate was increased once gas streaming occurred up to a maximum of 2 mL h^{-1}. The model crystalline system was found to be at 1 mL h^{-1} and 500 mbar air (see Section 3.1). Limited crystalline deformation was also analyzed for experimental conditions with less optimal bubble packing.

2.3 Image Analysis

MATLAB image processing of the recorded videos was used to determine the bubble properties (e.g. areas, centroid positions, and eccentricities) and foam properties (e.g. gas area fraction) for each experiment. Centroid positions were used to track bubbles and calculate instantaneous velocities. Voronoi diagrams were constructed to highlight crystalline deformation as dislocations located in the bulk of the crystal have a 5/7 nearest neighbor pair at the core (see Section 3.2). The convention used in the present work: 5-neighbor bubbles were colored blue, 7-neighbor bubbles were colored red, and 8-neighbor bubbles were colored green. Perfect packing for bubbles adjacent to a wall is 4 neighbors such that blue and red correspond to 3-neighbor and 5-neighbor wall bubbles respectively. Bubbles along the wall were manually colored accordingly due to limitations in the automatic extraction of the nearest neighbors from the Voronoi diagrams. Additional complications arose as 5-neighbor bubbles could remain within (see Fig. 9e,f) or enter (see Fig. 11d) the wall row without contacting the wall of the microfluidic channel. Therefore, these 5-neighbor bubbles have a surplus of neighbors (colored red) rather than the automatically identified deficit (colored blue) compared with perfect packing. Videos were reformed from the frames with colored bubbles for analysis of the crystalline phenomena. . The MATLAB particle image velocimetry[48] based toolbox PIVlab was utilized to measure instantaneous and averaged flow properties (e.g. velocity, strain rate, and shear rate) using black and white images.[49,50]

3 Results and discussion

3.1 Model crystalline system

The channel design supported characterization of crystalline deformation over a range of experimental conditions. In addition to limited dislocation interactions, a metric for defining packed crystalline systems was the presence of dislocation reflection in tension (by a similar mechanism as in the liquid-plate configuration[14]) in the expansion region of the central valley. Hereafter, “expansion” will refer to the central valley opposed to the region at the inlet of the wide channel. A high overall gas area fraction was required to offset the increased channel area in the expansion and the reduced nearest neighbors of wall bubbles. Thus, a packed crystalline system was defined as having a gas area fraction, $\Phi > \sim 0.93$. The highest gas area fraction achieved was 0.96, but these systems had larger, more deformable (i.e. less circular) bubbles that made these conditions less ideal for studying the full range of crystalline deformation phenomena. [51]

Recent microfluidic studies in a gradually tapering channel demonstrated that flowing, monodisperse emulsions exhibited ordered, cyclic dislocation glide and reflection in distinct regions where the number of droplet rows along a slip plane decreased by one.[26,51] In these localized sections of the channel the misorientation of the crystal is too high to be alleviated by the elastic deformation of the droplets. The independent “rearrangement zones” arise from the

resolved shear stress as the compressive stress is larger in the y-direction than in the x-direction (in the same convention as Fig. 1c, but with the y-axis centered around the constriction). The researchers outline five conditions, including monodispersity, required for spatiotemporal periodicity in the T1 topological rearrangements (see Section 3.2) corresponding to dislocation glide within a tapered channel geometry.[26,52] These criteria are evaluated in relation to the foam crystalline systems of the present work. The process of dislocation glide and reflection is cyclic in the expansion-contraction geometry, but the progressions do not maintain temporal long-range order. However, several common secondary dislocation phenomena foster (or do not impair) the cyclic deformation processes.

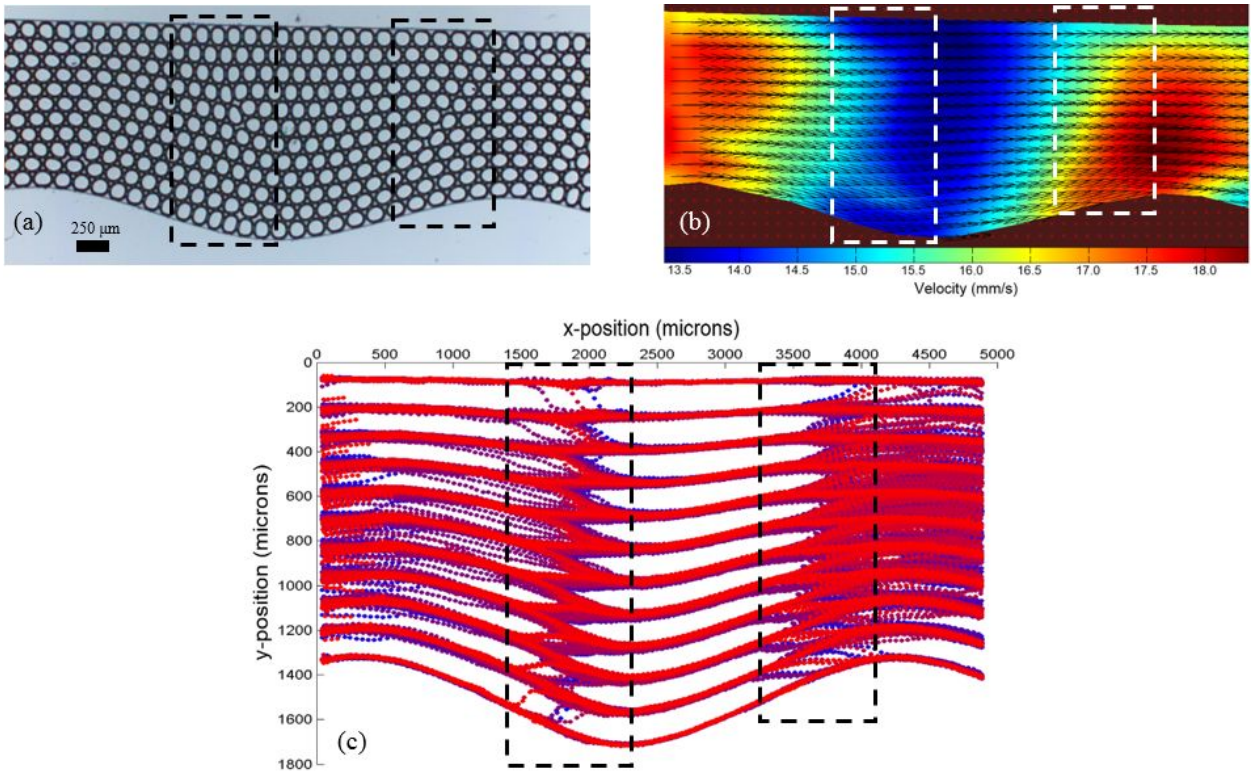

Fig. 1 Rearrangement zones[26] (marked by dash boxes) containing cyclic dislocation glide and reflection in tension (left) and compression (right). (a) The model crystalline system at 1 mL h^{-1} surfactant solution, 500 mbar air and $\Phi = 0.94$. A dislocation is gliding to the horizontal wall in the tension rearrangement zone and another is gliding towards the sinusoidal wall in the compression rearrangement zone. Scale bar of 250 μm corresponds to roughly two bubble diameters. (b) A representative average velocity plot of the model system generated in PIVlab.[49] The velocity profile transitions from nearly parabolic above the upstream peak to more plug-like within the rearrangement zones in accordance with the solid-like state of the foam.[51] The circular region of high velocity above the downstream peak is a nucleation hotspot (see Section 3.6). (c) Streamlines generated by overlaying centroid markers from one second (400 frames) of foam flow. The markers change from blue to purple to red as a function of recorded time. The large variance in bubble position and streamline forking prior to the valley and downstream peak corresponds with a transition of +1 and -1 in the number of bubbles in a column respectively.

Contrary to a succession of compression rearrangement zones,[26] a single tension rearrangement zone in series with a single compression zone (dashed boxes in Fig. 1, 5 and 6) was fostered by the gradual expansion and contraction of the wet foam through combination of a sinusoidal wall and a horizontal wall. These rearrangement zones were further probed to analyze the distinctive forms of dislocation glide (Section 3.3) and reflection (Section 3.4 and 3.5). The

average wall angle from peak to valley was approximately 11.3° with a maximum of 17.4°. The angle between the walls is in accordance with the maximum half angle of 8.2° for a tapered channel to prevent a high density of dislocations and undesired interactions.[26,52] Additionally, the spacing of ~8-10 bubble diameters between the rearrangement zones (see Fig. 4) enables the dislocation gliding in each region to act independently of one another, although a nucleation event can be triggered in a specific configuration of the dislocations (see Fig. 13). For the crystalline systems studied, the number of bubbles in an alternating column (i.e. a zig-zag configuration opposed to a diagonal configuration along a slip plane[26]) ranged from 9-13 over a peak and 10-15 over a valley with the typical differential being a single bubble. The rearrangement zones can be prevented in systems with $\Phi \sim 0.96$ as cyclic dislocation glide and reflection does not occur when bubbles are large enough to span the peak and valley regions with the same number of bubble rows. The optimal packed system was found to be at 1 mL h^{-1} surfactant solution, 500 mbar air and $\Phi = 0.94$ with the bubbles in a column transitioning from 11 over a peak to 12 over a valley (Fig. 1a, ESI† Videos 1 and 2). The width of 12 bubble diameters for the foam crystal is consistent with the upper bound of more dynamically controllable emulsion crystals, but the packing fraction is just beyond the $\sim 0.80 < \Phi < \sim 0.92$ necessary to preserve hexagonal packing in the tapered channel geometry.[26,52]

In the model crystalline system, the velocity profile transitions from nearly parabolic above the upstream peak to more plug-like within the rearrangement zones (Fig. 1b). Taking the characteristic length l as the minimum width of the channel and the characteristic velocity U from the bubbles in the contraction region, $\mathrm{Re} = \rho Ul/\mu \sim 30$ and $\mathrm{Ca} = \mu U/\sigma \sim 10^{-4}$, where ρ, μ, and σ is the density, dynamic viscosity, and surface tension of the surfactant solution respectively. Bubbles within the monodisperse foam primarily follow the streamlines with significant departure in the two regions where bubble column length changes (Fig. 1c). All of these properties signify the solid-like state of the flowing foam. The final criterion from previous emulsion crystal studies is that $\mathrm{Ca} < \sim 10^{-2}$ at the constriction in order for the spatial distribution of T1 events to remain localized in distinct rearrangement zones.[26,52] The researchers observed that dislocations move horizontally by successive T1 events along the primary direction of flow as the emulsion transitions to a liquid-like state, which disrupts the dynamics of the dislocations gliding within the rearrangement zones. Recently the liquid-like regime of the monodisperse emulsion system was reclassified to be in the range of $10^{-3} < \mathrm{Ca} < 10^{-2}$, with the foam crystalline systems of the present work corresponding to the solid-like subregime where frictional forces between bubbles are significant (i.e. regime 2, $10^{-6} < \mathrm{Ca} < 10^{-3}$).[51]

The frequency of the T1 topological rearrangements responsible for dislocation glide (and the additional dislocation mechanisms observed) was analyzed for the model crystalline system. T1 events occurred 766.2 ± 80.9 s^{-1} (1.92 ± 0.20 per time interval at 400 fps). A scaled T1 event count (the number of T1 events per bubble) was defined as $P_{T1} = N_{T1}/N_{bubbles}$ in a similar fashion as previously performed for drops in a tapered microfluidic channel.[51] However, a major difference in the present calculation compared with the previous emulsion work was that the control volume for observing the number of T1 events and advected bubbles was the length of the channel from peak to peak rather than an individual rearrangement zone (see ESI† Fig. S1 for additional information on the calculation of P_{T1}). $P_{T1} = 0.33 \pm 0.03$ for the foam generated at 1 mL h^{-1} surfactant solution, 500 mbar air.

3.2 Dislocation theory and T1 topological rearrangements

Considerable information can be found about edge dislocations,[53] but some fundamental topics will be subsequently noted.[14,26] A hexagonally packed crystal lattice has three close-packed directions in a 2-D plane at 120° intervals with the convention herein that direction 1 is parallel to the horizontal wall and positive against the foam flow (Fig. 2a). More accurately, direction 1 is aligned with the streamlines of the flowing bubbles comprising a perfect crystal, which may have curvature depending on the location within the channel (Fig. 1a,c). As shown in Fig. 2c, the relative positioning of the close-packed directions within defect-free areas of the flowing crystal is distorted by the expansion-contraction flow.

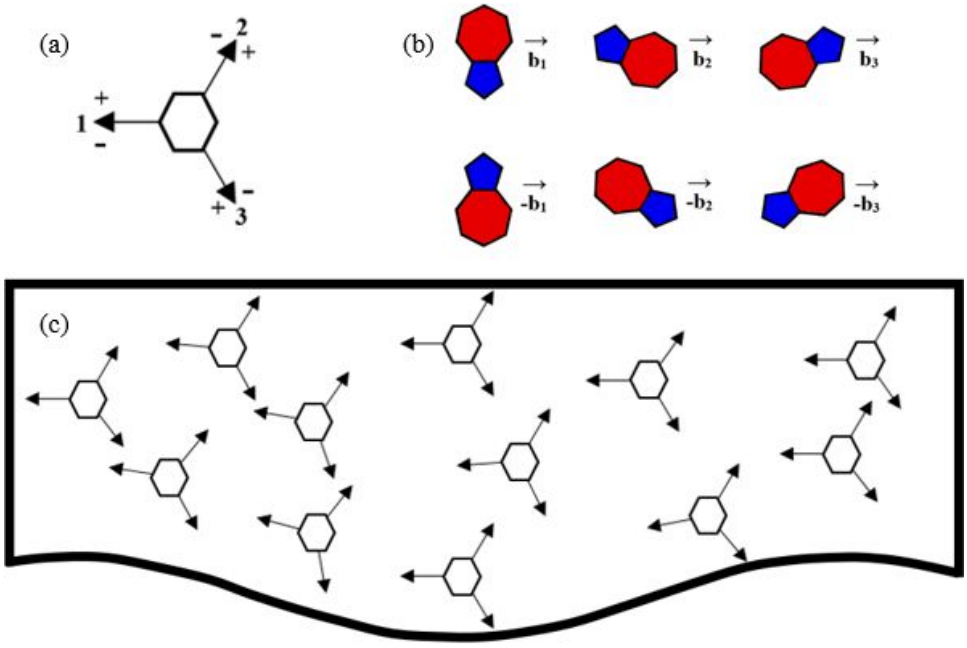

Fig. 2 (a) Three close-packed directions at 120° intervals for a 2-D hexagonally packed crystal lattice. (b) Idealized 5/7 nearest neighbor pairs with corresponding Burgers vectors along the closed-packed directions. (c) Representative closed-packed directions in defect-free regions of the model crystalline system undergoing expansion-contraction flow. The hexagonally packed crystal is not distorted near the walls in the region around the maximum expansion of the channel. Distortions in the first direction occur from the curvature of the bubble rows aligned with the sinusoidal wall. The greatest distortions occur in the curved rows within the regions surrounding the inflection points of the sinusoidal wall. The compression of the crystal in the regions around the contractions results in distortions in the third direction.

The Burgers vector gives the magnitude (scaling with the bubble diameter) and direction of the crystal lattice distortion (the pair of extra half-rows being in the other two directions). At the core of a dislocation is a 5/7 nearest neighbor pair connected along the Burgers vector (Fig. 2b). The sign of the dislocation is given by the orientation of the 5/7 neighbor pair with a positive dislocation having the seven-neighbor bubble positioned clockwise from the positive orientation of the close-packed direction containing the Burgers vector.[14] Dislocation glide is the movement of a dislocation on the slip plane containing the Burgers vector, which primarily occurs at 60° relative to the horizontal wall in the present work. The resistance to dislocation motion is the Peierls-Nabarro stress, the inherent lattice friction of the crystalline structure, which decreases with increasing distance between the rows of bubbles comprising the crystalline lattice.[53]

Elementary T1 topological rearrangements are central to the crystalline deformation described herein. The stages of the T1 process for a two dimensional wet foam were recently illustrated in the study of pipe flow.[23] The T1 process consists of neighbor switching between four bubbles such that two initially adjacent bubbles diverge as the other two secondary neighbor bubbles converge. When modeled as a dry foam (or equivalently as a Voronoi diagram), the rearrangement is the result of an edge length reducing to zero and four films meeting at a single point. Although the T1 process for wet foam is not instantaneous, the number of T1 events per bubble per unit strain in a steady shear system has been shown to be insensitive to gas area fraction between 0.85 to 1.[54] The shearing of two bubble lanes along a close-packed direction is the means of dislocation glide *via* successive T1 topological rearrangements termed T1 cascades (Fig. 3).

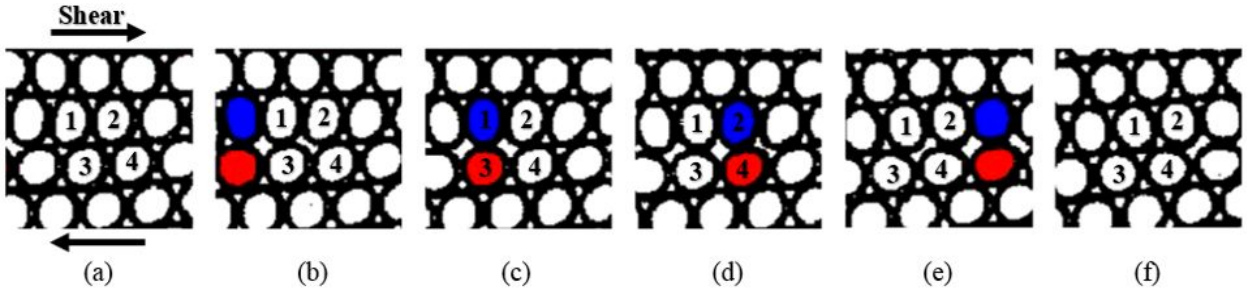

Fig. 3 The stages of the T1 process for a 2-D wet foam. Neighbor switching occurs as two initially adjacent bubbles (2,3) diverge as the other two secondary neighbor bubbles (1,4) converge. As the T1 rearrangement progresses, a $-\vec{b}_1$ dislocation glides from left to right. (b-e) For wet foam, the four films undergo several different configurations.

Dislocation interactions complicate an otherwise simple system for observing plastic deformation. These interactions were most prevalent in the more disordered (lower gas area fraction) systems than the model system and will not be discussed in detail. The primary form of these interactions was dislocation reaction, i.e. the combination of two or three dislocations by vector addition of the Burgers vectors. Thus, the combination of dislocations of matching sign in each close-packed direction is an annihilation reaction resulting in perfect packing.

3.3 Dislocation glide

The use of an asymmetric channel in expansion-contraction flow enhances the study of dislocation glide. The process is itself asymmetric as dislocation glide originating from the sinusoidal wall results in misalignment or curving of the bubble rows whereas glide away from the horizontal wall leads to realignment or straightening. Fig. 4 illustrates the relative curvature of a central bubble row at two different states of the model crystalline system compared to a reference black bar for a horizontal bubble row. Fig. 4a (ESI† Video 1) depicts the misaligned state after gliding dislocations have moved through the central row towards the horizontal wall in both rearrangement zones. Fig. 4b (ESI† Video 2) illustrates the more aligned condition once a gliding dislocation has straightened the row in the tension rearrangement zone and prior to misalignment in the compression rearrangement zone.

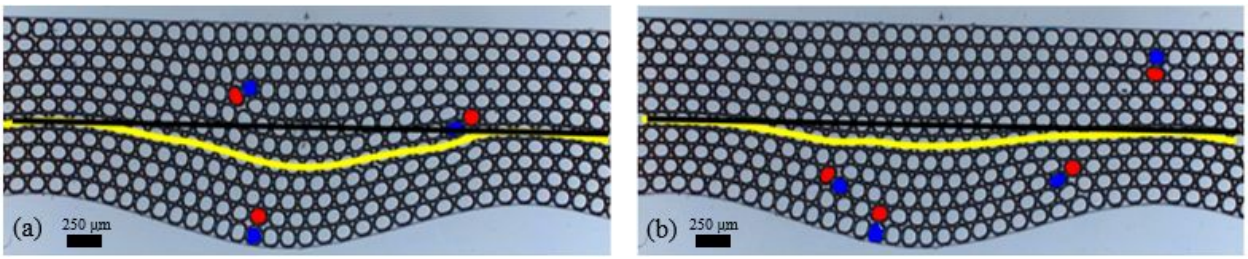

Fig. 4 Comparison of the relative curvature of a central bubble row marked in yellow in the (a) misaligned state and (b) aligned state. The upper black bars correspond to the analogous straight bubble row (the slight downward slope of the wall is due to the orientation of the device). The maximum misalignment is roughly (a) two bubble diameters (nearly 80% of the average wall angle from peak to valley) and (b) one bubble diameter (under 40% of the average wall angle). Experimental conditions:1 mL h^{-1}, 500 mbar and $\Phi = 0.94$.

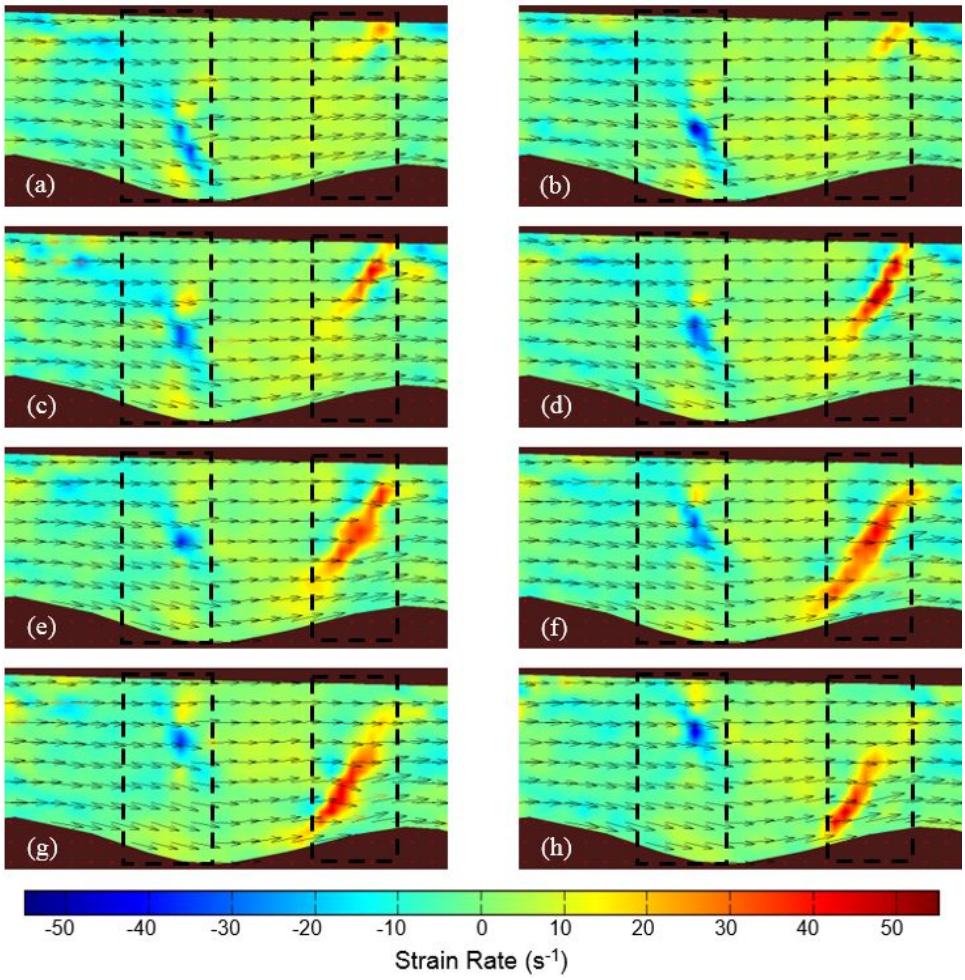

Fig. 5 Strain rate of gliding dislocations in the tension and compression rearrangement zones (marked by dashed boxes) in between reflections at the wall. (a-h) The localized dislocation in tension (blue) remains at a nearly constant x-position within the channel while gliding towards the horizontal wall. (c-h) The gliding dislocation in compression (red) stretches across multiple bubble rows assisted by the extended misalignment of the bubble rows away from the horizontal wall. Plots are generated in PIVlab with every other vector displayed for visual clarity.[49] Strain rates are calculated as $\partial u/\partial x - \partial v/\partial y$, the strength of the velocity gradient along the direction of the local velocity.[48] Elapsed time between images is 2.5 ms. Experimental conditions:1 mL h^{-1}, 500 mbar and $\Phi = 0.94$.

The asymmetry of the crystalline alignment fundamentally dictates the dislocation dynamics. Dislocations gliding towards the horizontal wall remain localized, being unable to penetrate multiple aligned bubble rows (Fig. 5,6 for the dislocation in the tension and in the compression rearrangement zone respectively). The dislocation gliding in tension away from the horizontal wall becomes more localized with the associated strain rates reducing from between –40 and –50 s^{-1} to between –10 and –20 s^{-1} as the bubble rows near the sinusoidal wall cannot be straightened (Fig 6). The strain rates for the flowing foam are one to two orders of magnitude greater than those previously estimated for a monodisperse emulsion system in a tapered microfluidic channel.[26]

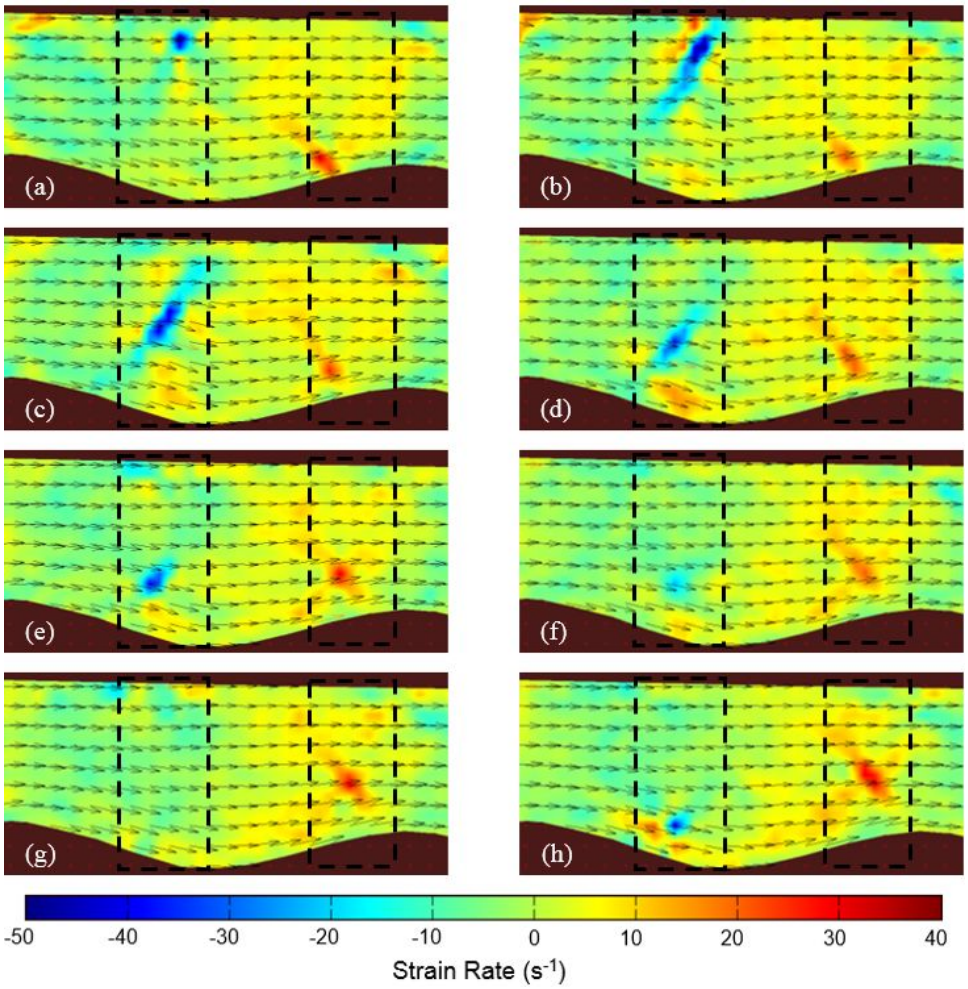

Fig. 6 Strain rate of gliding dislocations in the tension and compression rearrangement zones (marked by dashed boxes) in between reflections at the wall. (b,c) The gliding dislocation in tension (blue) stretches across multiple bubble rows while pulling misaligned bubble rows into alignment. (g) Strain rate is negligible before (h) the reflection process begins at the sinusoidal wall. (a-h) The localized dislocation in compression (red) moves in a stick-slip manner due to the increasing Peierls-Nabarro stress from the increasing alignment of the bubble rows. The discontinuous glide results in the bubbles comprising the dislocation being advected downstream while traveling towards the horizontal wall. Plots are generated in PIVlab with every other vector displayed for visual clarity.[49] Strain rates are calculated as $\partial u/\partial x - \partial v/\partial y$, the strength of the velocity gradient along the direction of local velocity.[48] Elapsed time between images is 5.0 ms. Experimental conditions:1 mL h^{-1}, 500 mbar and $\Phi = 0.94$.

The compression rearrangement zone has the greatest dichotomy in dislocation glide. Strain rates for glide away from the horizontal wall reach as high as 60–65 s^{-1} (Fig. 5d) as the plastic deformation is facilitated by the extended misalignment of the bubble rows. The dislocation can travel over 500 μm (4 bubble diameters) upstream before reaching the wall bubbles at the sinusoidal wall. In contrast, glide away from the sinusoidal wall is discontinuous with the x-position of the dislocations drifting downstream due to the foam flow (Fig. 6). The increasing Peierls-Nabarro stress from the increasing alignment of the bubble rows leads to stick-slip dislocation movement. The dislocation velocity along the width of the channel is two to three times smaller and the duration of glide between reflections is over three times as long.

3.4 Dislocation reflection in tension

The expansion created by the sinusoidal wall subjects the foam to tension and we will first focus on reflections that occur at the horizontal wall. For packed crystalline systems ($\Phi > \sim 0.93$), dislocation glide in the negative third direction (i.e. partially against flow) can result in conservative reflection. Three different profiles of conservative reflection in tension were observed. The first reflection, comparable to the one observed by Rosa and Fortes,[14] will be termed the standard reflection. The seven-neighbor (red) bubble of the gliding dislocation retreats into the bulk upon reaching the bubble row at the wall, which extends the (starred) wall bubble positioned along the slip plane (Fig. 7a-c). The dislocation reaches the wall as a $5_w/3_w$ pair (Fig. 7c) and reflects conservatively (Fig. 7d). The conservative reflection can be expressed as $\vec{b}_3 \rightarrow -\vec{b}_1 - \vec{b}_2$.

As the reflected dislocation glides into the bulk, the bubbles converge in the interstitial space between the wall row and the adjacent row. The extended wall bubble is forced against the wall and the $3_w/7$ dislocation shifts back along the positive first direction (Fig. 7e,f) before moving along the wall against flow. The dislocation at the wall glides opposite the direction of the Burgers vector (see Fig. 3) due to the local flow conditions as bubbles in the wall row move slower than those in the adjacent row. Another difference from the reflection in the bounded liquid-plate configuration[14] is the shifting of the dislocation positioned at the wall, which aligns the seven-neighbor bubbles of each dislocation along the same side of the slip plane of the reflected dislocation (Fig. 7f). The shifting of the wall dislocation is a function of the reduced bubble packing density at the wall, rather than the flow conditions governing the subsequent dislocation movement (see Section 3.4.3).

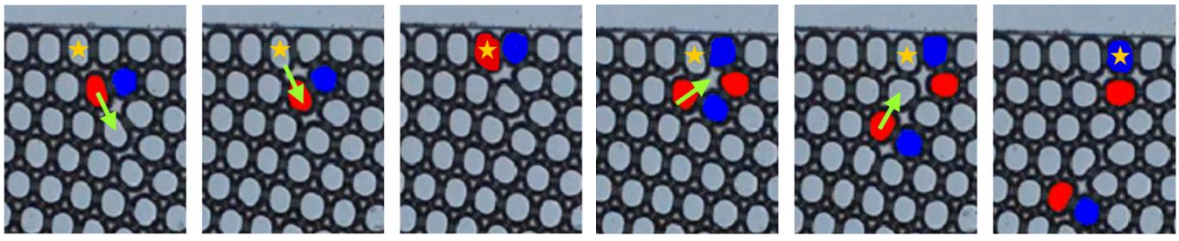

Fig. 7 The standard reflection in tension at the horizontal wall (see ESI† Video 2 for the standard reflection at the sinusoidal wall). The reflection is conservative as a dislocation is left at the wall and a dislocation glides back into the bulk. (not shown) The dislocation at the wall glides in the same lateral direction (i.e. against flow) as the reflected dislocation, contrary to reflection in the liquid-plate configuration[14] and dislocation reflection far from the horizontal wall (see Section 3.4.3). Experimental conditions:1 mL h^{-1}, 500 mbar and $\Phi = 0.94$ with elapsed time of 22.5 ms (where two bubble diameters correspond to roughly 250 μm).

The other two reflection profiles (also occurring in systems with higher Φ than the model crystalline system) are the result of the higher local packing density of the wall row. Specifically, the (starred) wall bubble positioned along the slip plane is less elongated (as measured by the y-coordinate of the centroid) at the time the gliding dislocation reaches the bubble row at the wall as well as throughout the reflection process. As such, the gliding dislocation never reaches the wall as a $5_w/3_w$ pair despite the convergence of bubbles as in the standard reflection. These profiles will be termed "dislocation-union" and "dislocation-split" reflections. For dislocation-union reflections (Fig. 8a-e), the analogous (starred) wall bubble extends without impeding the converging bubbles. A temporary union forms with the reflected dislocation and the dislocation at the wall sharing a single eight-neighbor bubble (Fig. 8d). For dislocation-split reflections (Fig. 8i-v), the extending bubble is adjacent to the analogous (starred) wall bubble in the direction of flow (Fig. 8iii). The reflected dislocation originates at the wall (Fig. 8iv) instead of in the adjacent row (Fig. 7d and 8d). The equivalent eight-neighbor bubble is subsequently shared as in dislocation union reflection, although the configuration was often to transitory to be recorded at 400 fps. In both cases, the dislocation at the wall is generated at the final position rather than shifting back along the positive first direction as in the standard reflection.

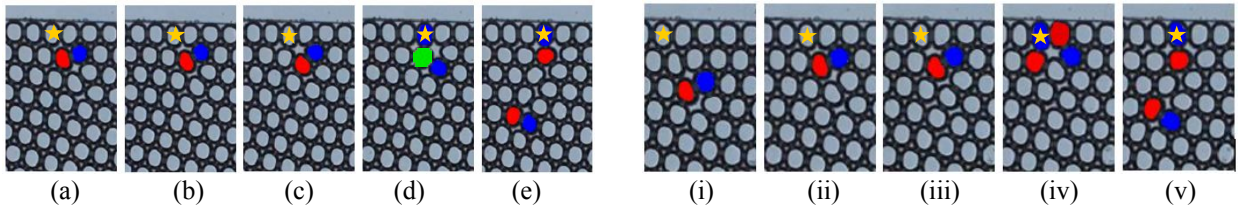

Fig. 8 (a-e) The dislocation-union reflection and (i-v) dislocation-split reflection in tension (elapsed time 15 ms for each sequence). In both cases, the final configuration of the dislocations is identical to the standard reflection. Experimental conditions:1 mL h^{-1}, 500 mbar and Φ = 0.94 (where two bubble diameters correspond to roughly 250 μm).

3.4.1 Hopping. Rosa and Fortes coined the term "hopping" in relation to the phenomenon subsequently described.[14] The researchers noted that dislocation reflection in tension resulted in high energy free space (in the form of large Plateau borders for dry foam) between the wall row and adjacent row since the latter shrinks from the retreating bubble. A bubble may hop from the wall row into the adjacent row to return the system to the close-packed configuration, and successive hopping occurred with the equivalent appearance of a gliding dislocation. Therefore, these events were viewed as distinct from gliding dislocations and no further information was given regarding the timing of hopping.[14] In the present system, hopping occurs in place of a conservative reflection in tension. Hopping was the only form of reflection in the expansion when Φ < ~0.93 due to the reduced packing density of bubbles near the wall row. Additionally, only hopping occurred when the dislocation approaching the horizontal wall was gliding in the positive second direction (i.e. partially with flow) as the result of an undesired dislocation reaction. In fact, hopping was the most commonplace mechanism (>50%) at the horizontal wall in the tension rearrangement zone of the model system (ESI† Video 2).

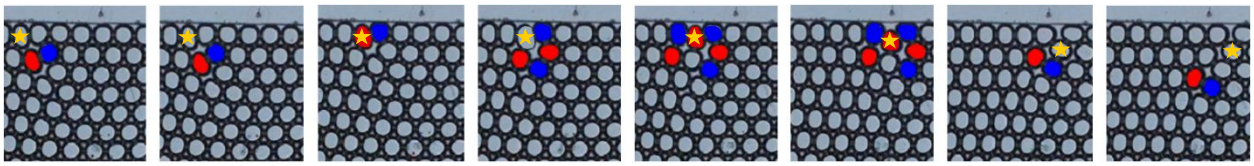

Fig. 9 (a-d) Reflection in tension is replaced by (e-h) non-conservative hopping where a wall bubble displaces into the adjacent row of bubbles to return the system to the close-packed configuration (elapsed time 50 ms). (e-f) The surrounding dislocations around the (starred) $5_w/3_w$ dislocation are extraneous as (g-h) perfect packing is restored at the wall and in the adjacent row once hopping is completed. The bubble displaced from the second row by the hopped bubble becomes the five-neighbor bubble of the resulting dislocation. The reflected dislocation shifts one bubble in the positive first direction due to the hopping bubble (note the relative location of the starred bubble to the slip plane of the reflected dislocation in g *vs*. d). Experimental conditions:1 mL h^{-1}, 500 mbar and $\Phi = 0.94$ (where two bubble diameters correspond to roughly 250 μm).

Hopping at the horizontal wall starts analogously to the standard reflection (Fig. 9a-d) prior to the extended (starred) wall bubble displacing into the free space in the adjacent row (Fig. 9e). The (starred) hopping bubble remains part of the $5_w/3_w$ pair with $\vec{b}_3$ orientation while entering the adjacent row (Fig. 9e,f *vs*. Fig. 9c). The reflected dislocation is formed as the hopped bubble displaces a bubble from the adjacent row into the third row (Fig. 9f,g). Thus, hopping at the horizontal wall results in the non-conservative reflection of $\vec{b}_3 \rightarrow -\vec{b}_2$ as no $\vec{b}_1$ dislocation is left at the wall. The reflected dislocation is shifted one bubble in the positive first direction compared with the standard reflection. The nearby dislocations in Fig. 9e,f are not part of the overall reflection and these configurations were often to transitory to be recorded at 400 fps.

3.4.2 Dislocation reflection in tension at sinusoidal wall. Reflection in tension or hopping can take place at the sinusoidal wall with the most commonplace event (>50%) being a combination of both (ESI† Video 1). A $\vec{b}_1$ dislocation formed upon reflection at the sinusoidal wall will oscillate around a central position upstream of the base of the valley (see Fig. 4a,b). The sinusoidal wall acts a well with the relatively static position of the dislocation due to the competing forces of dislocation glide and advection of the bubbles comprising the dislocation. Dislocation glide against flow is hindered by the curvature of the bubble rows near the sinusoidal wall as the Burgers vector is increasingly misaligned with the close-packed direction of bubbles (see Fig. 2c). Near the base of the valley, dislocation glide is facilitated due to the straighter bubble rows and the increased free space from the reduced elongation of the wall bubbles (see Fig. 4a,b). Once a $-\vec{b}_2$ gliding dislocation reaches the wall bubble row, an interaction with the trapped $\vec{b}_1$ dislocation (when present) generally ensues. Glide of the trapped dislocation (assisted by the free space around the $-\vec{b}_2$ dislocation) is sufficiently fast in the model system to disrupt the reflection process even when the trapped dislocation is located multiple bubbles downstream. A multi-stage reflection in tension at the sinusoidal wall in the model system is displayed in further detail (ESI† Fig. S2).

3.4.3 Dislocation reflection in the bulk. Reflection in tension can transpire away from a wall and this phenomenon occurs when a dislocation is gliding into a region of crystalline alignment (e.g. the portion of the channel above the black reference bars in Fig. 4). In the model system, this mechanism prevents ~25% of the dislocations gliding towards the horizontal wall from reflecting at the wall (ESI† Video 1). Fig. 10 highlights how reflection can occur several bubble rows away from a wall. Dislocation glide is depicted in Fig. 10a,b wherein the seven-

neighbor bubble moves against the gliding direction. The effective edge length between bubbles 2 and 3 reduces to zero as a T1 topological rearrangement occurs in the interstitial space ahead of the gliding dislocation. A different T1 topological rearrangement occurs between Fig. 10b and Fig. 10d similar to the standard reflection in tension (see Fig. 7c,d). The bubbles behind the gliding dislocation converge in the interstitial space and cause bubble 1 to no longer neighbor bubble 3 contrary to the case of dislocation glide.

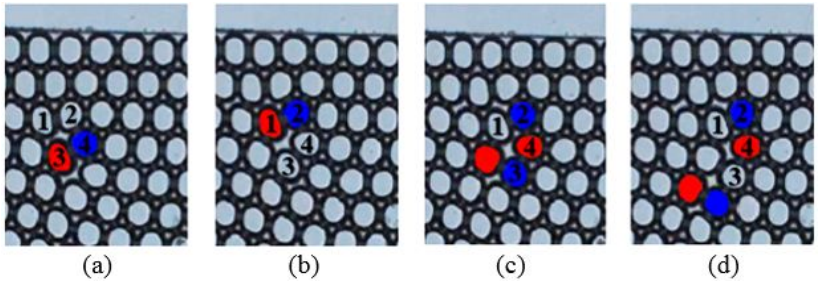

Fig. 10 (a,b) Dislocation glide where bubble 3 has retreated into the bulk in the same manner as the seven-neighbor bubble in Fig. 7a,b. (b-d) Dislocation reflection in the bulk (elapsed time 15 ms) where the (unlabeled red) bubble in the negative second direction of bubble 1 converges with bubble 4. Dislocation glide would have resulted in bubble 1 moving analogously to bubble 3 with the two bubbles remaining neighbors. Dislocation reflection in the bulk can occur when a dislocation is gliding into a region of crystalline alignment. Experimental conditions:1 mL h^{-1}, 500 mbar and $\Phi = 0.94$ (where two bubble diameters correspond to roughly 250 μm).

In the standard reflection, the (starred) wall bubble in the analogous position to bubble 1 is forced against the wall by the motion of the bubbles opposite of the direction of reflection (see Fig. 7d-f). For reflection in the bulk, bubble 1 can remain offset relative to bubble 2 in the y-direction (Fig. 10d), which prevents the $-\vec{b}_1$ dislocation from shifting back along the positive first direction as in the standard reflection. The $-\vec{b}_1$ dislocation glides against flow (as in reflection in tension) when spanning the second and third rows from the horizontal wall. Farther in the bulk, the dislocation moves with flow from a combination of dislocation glide and advection of the bubbles comprising the dislocation until a breakup reaction occurs from the compressive forces in the region of the contraction (as demonstrated in ESI† Fig. S3 for the model system). The initial shift against flow of the $-\vec{b}_1$ dislocation has been observed prior to the dislocation moving with flow, supporting the shifting action as separate from dislocation movement against flow for the case of the standard reflection (see Fig. 7e,f).

The strain rate profile (as calculated in PIVlab[49]) around the gliding dislocation prior to reflection in the bulk corresponds with that of a dislocation which continues gliding towards the horizontal wall. Thus, reflection in the bulk occurs primarily due to the local packing of bubbles around the gliding dislocation. The dislocation gliding towards the horizonal wall in the tension rearrangement zone is intermittently out of ideal alignment. The angle between the y-axis and 5/7 dislocation pair reaches as high as 70° opposed to 60° (note the higher angle between the centroids of bubbles 1 and 2 in Fig. 10b compared with bubbles 3 and 4 in Fig. 10a). Dislocation glide can temporarily stall as the seven-neighbor bubble moves against the gliding direction into the optimal configuration. The temporary lapse in dislocation glide is not sufficient for dislocation reflection in the bulk to occur. The process of reflection in the bulk is aided by the increasing alignment of the bubble rows near the horizontal row. The alignment resists dislocation glide due to the increased Peierls-Nabarro stress and facilitates the convergence of bubbles behind the dislocation due to the decreased curvature of the rows with respect to the rows near the sinusoidal wall.

Specifically, the bubbles behind the dislocation are more aligned along the direction of flow as the dislocation approaches the horizontal wall. More research on the localized factors leading to dislocation reflection in the bulk needs to be conducted to elucidate any predictive measures.

3.5 Dislocation reflection in compression

The foam is subjected to compression upon exiting the expansion from the contraction generated by the sinusoidal wall. There is no difference in the mechanism of reflection for the horizontal wall and the sinusoidal wall. The reflection profile is equivalent to the one first outlined by Rosa and Fortes[14] and observed for an emulsion in a tapered microfluidic channel.[26] The wall bubble along the glide direction of the seven-neighbor bubble extends into the free space around the dislocation (Fig. 11b). The gliding dislocation becomes a $5_w/5$ pair and the adjacent (starred) wall bubble in the positive first direction adopts a horizontally elongated, elliptical orientation from the vacated space and the compressive forces in the contraction (Fig. 11c). The five-neighbor bubble of the gliding dislocation and the elliptical (starred) bubble become a $5_w/3_w$ pair as the wall row gains a bubble (Fig. 11d,e). The resulting dislocation reflection is not conservative and can be expressed as $-\vec{b}_3 \rightarrow \vec{b}_2$ for the horizontal wall. As discussed in Section 3.4, conservative reflection in tension creates a dislocation at the horizontal wall that glides against flow. Prior to reflection at the horizontal wall, the dislocation gliding in the compression rearrangement zone can combine by vector addition with the dislocation gliding along (or near) the wall that resulted from reflection in tension at the wall (or in the bulk) downstream. The reaction can be expressed as $-\vec{b}_3 + -\vec{b}_1 \rightarrow \vec{b}_2$ and creates an equivalent dislocation as reflection in compression. Less commonly the identical reaction takes place with the $-\vec{b}_1$ dislocation originating from upstream reflection in the bulk (see Section 3.4.3). These reactions prevent >~50% of the dislocations gliding towards the horizontal wall from reflecting in compression (ESI† Video 2). For the sinusoidal wall, the slope causes the process of the wall row gaining a bubble during reflection in compression to occur almost horizontally (see Fig. 1c for the centroid positions between the bottom two streamlines in the compression rearrangement zone).

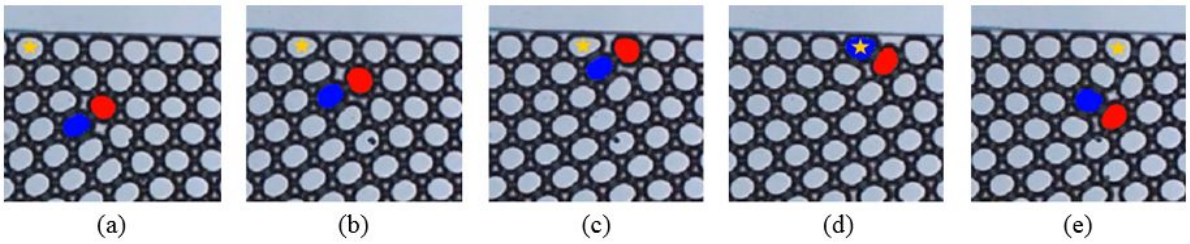

Fig. 11 Reflection in compression at the horizontal wall (elapsed time 40 ms). (c-d) Once the gliding dislocation reaches the wall, the (blue) five-neighbored bubble with less than six nearest neighbors becomes a (red) five-neighbored wall bubble with more than four nearest neighbors. (d-e) Thus, the reflected dislocation is formed, but the reflection is not conservative as no dislocation is left at the wall. Experimental conditions:1 mL h^{-1}, 500 mbar and $\Phi = 0.94$ (where two bubble diameters correspond to roughly 250 μm).

3.6 Dislocation nucleation

In addition to being the mechanism of dislocation glide, T1 topological rearrangements in an area of perfect crystal lead to homogeneous dislocation nucleation. The most frequent and fundamental in the present system is $\vec{b}_2$ dislocation nucleation. These nucleation events are analogous to those

observed from nanoindentation of a bubble raft, wherein a positively and negatively oriented dislocation pair form at four neighboring bubbles and separate by gliding in opposite directions.[18,19] In the microfluidic system, the peak of the sinusoidal wall acts as the indenter.

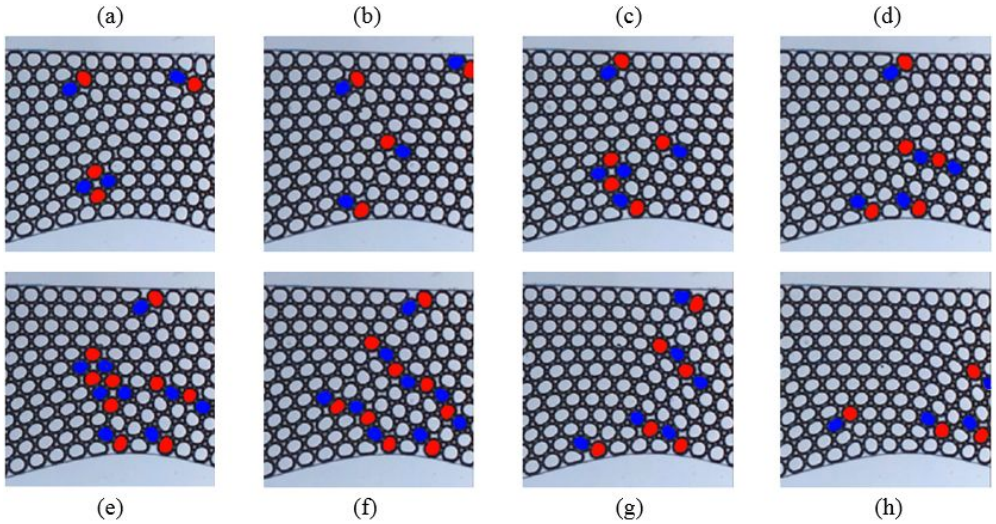

Fig. 12 Multiple $\vec{b}_2$ nucleation events in the region of the contraction. These events occur due to the reduction of bubbles in an alternating column (12 to 11 in the model system shown above) taking place in upstream proximity of the peak (within two bubble diameters). The dislocation pairs separate as the seven-neighbor (red) bubbles converge along the direction of compression. (a,b) A $\vec{b}_2$ nucleation event followed by (c,d) a coupled event and (e) a subsequent pair of events. (f) Grain boundaries around an area of misaligned crystal are briefly formed. (g-h) The $-\vec{b}_3$ dislocation observed near or at the horizontal wall in (a-f) reflects several bubble diameters downstream of the peak and is annihilated by a nucleated dislocation from the final event. The opposite dislocation of the final event reflects off the sinusoidal wall, which restarts the cyclic reflection in compression process (elapsed time 75 ms). Experimental conditions:1 mL h^{-1}, 500 mbar and $\Phi = 0.94$ (where two bubble diameters correspond to roughly 250 μm).

As demonstrated in Fig. 12, $\vec{b}_2$ nucleation occurs in a localized region immediately prior to a peak (within two bubble diameters). A nucleation event is triggered when the reduction of bubbles in an alternating column occurs at the downstream end of the compression rearrangement zone (Fig. 12a,b). Bubbles in the misaligned crystal near the sinusoidal wall adopt a horizontally elongated, elliptical orientation as the longer bubble column is squeezed within the region of the contraction. The local packing density is reduced, and the bubbles preferentially converge along the direction of compression. Strain rates prior to the T1 topological rearrangement responsible for nucleation were calculated[49] between 15–25 s^{-1} in the model system. The initial nucleation event only transpires when the crystal around the contraction is misaligned, predominately for the model system when the dislocation undergoing cyclic compression is gliding towards the horizontal wall and within 0-2 rows of the wall bubbles (Fig. 12a). The glide away from the horizontal wall after a reflection in compression and the resulting reduction of rows in the region of the contraction inhibits $\vec{b}_2$ nucleation as the transition in bubble column length takes place farther upstream.

These nucleation events often occur in pairs along adjacent slip planes with the sequence occurring against flow and 0-2 rows above the previous nucleation (Fig. 12c,e). The subsequent events are induced in the same manner as the initial nucleation (note the relative position along the direction of flow for the nucleation events in Fig. 12a *vs*. Fig. 12e). Strain rates from these nucleation events were calculated[49] between 30–60 s^{-1} in the model system. Nucleation ceases once a dislocation reflects in compression off the sinusoidal wall (Fig. 12g,h). Thus, $\vec{b}_2$ nucleation acts

as a source of the dislocation that undergoes cyclic reflection in compression, replacing the preceding dislocation at the horizontal wall that is either annihilated after a delayed reflection (Fig. 12g,h) or unable to reflect due to insufficient compressive forces after the contraction. The compression rearrangement zone is not disrupted when $\vec{b}_2$ nucleation occurs simultaneously or immediately following the reflection in compression at the horizontal wall (ESI† Video 1). In the model system, $\vec{b}_2$ nucleation occurs with roughly the same frequency as dislocation reflection at the horizontal wall in the compression rearrangement zone.

The $\vec{b}_1$ nucleation events occur in a localized area between the rearrangement zones across experimental conditions (Fig. 13) due to the interplay between the otherwise independent gliding dislocations. First, the dislocation in the compression rearrangement zone reflects at the sinusoidal wall. As the row of bubbles along the wall gains a bubble and the dislocation reflects, a rapid downward shift of bubbles along the slip plane of the reflected dislocation occurs. The extent of this shifting determines the relative y-position of the $\vec{b}_1$ nucleation (primarily the fourth and fifth bubble rows from the sinusoidal wall irrespective of bubble size). The $\vec{b}_1$ nucleation events are not as frequent as $\vec{b}_2$ nucleation events, requiring the dislocation in the tension rearrangement zone to pass through the corresponding rows of bubbles at approximately the same time as the dislocation in the compression zone.

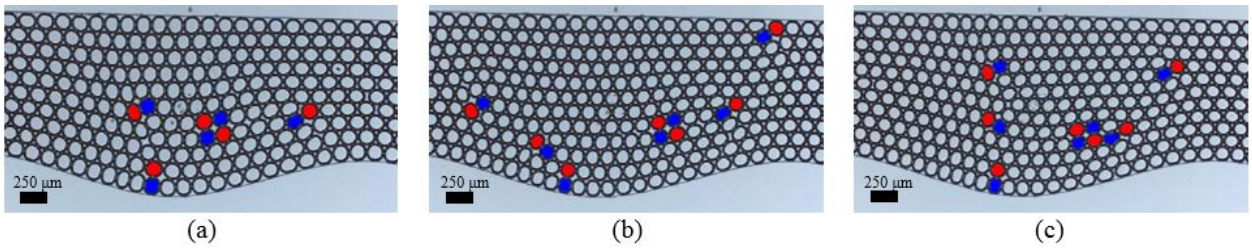

Fig. 13 A $\vec{b}_1$ nucleation event due to the interplay between the dislocation gliding from compression and the one gliding from tension across various experimental conditions. Following nucleation, the $\vec{b}_1$ dislocations separate by gliding in opposite directions and may react with the dislocations gliding under tension and compression. (a) 0.45 mL h^{-1}, 300 mbar and $\Phi = 0.93$; 10 to 11 bubbles in an alternating column from peak to valley. (b) 0.75 mL h^{-1}, 400 mbar and $\Phi = 0.93$; 10 to 12 bubbles. (c) 1 mL h^{-1}, 500 mbar and $\Phi = 0.94$; 11 to 12 bubbles.

The mechanism of nucleation is unchanged whether the dislocation undergoing tension is gliding towards the horizontal or sinusoidal wall (Fig. 13a *vs*. 13b,c). The shearing of these rows is the result of the dislocation in the tension rearrangement zone creating excess free space from the altered alignment of the rows. The direction of the gliding motion does not impact the $\vec{b}_1$ nucleation event since the top row is either straightened (shortened) first as the dislocation glides to the sinusoidal wall or curved (lengthened) second as the dislocation glides towards the horizontal wall. Thus, the top row is accelerated across the row below in both cases (as in Fig. 3). Shear rates from these nucleation events were calculated[49] as high as $-45\ s^{-1}$ in the model system. These nucleation events do not fundamentally alter the system as reactions with the dislocations gliding under tension and compression merely switch the subsequent reflection to the opposite wall.

3.7 Dislocation dipoles

The approach of two dislocations of opposite Burgers vector on a slip plane results in an annihilation reaction and the restoration of perfect packing. A dipole is formed upon collision when the approaching dislocations are on adjacent slip planes. Herein, dipoles will be referred to by the neighboring bubbles, e.g. 7/7 dipoles have the seven-neighbor bubbles sharing a common edge. Dipoles were observed across a range of experimental conditions, and conditions with gas area fractions greater than the value of $\Phi = 0.94$ for the model system will be presented. As dipoles have reduced local packing densities, studies were conducted at the highest attainable Φ to ensure adequate characterization of the temporal progression of dipoles in a crystalline environment.

3.7.1 7/7 dipoles. 7/7 dipoles formed in the expansion region following irregular dislocation events. In Fig. 14, the oppositely oriented $\vec{b}_3$ dislocations were created as a result of (otherwise undesirable) dislocation interactions over the upstream contraction. 7/7 dipoles do not resemble the Stone-Wales (SW) defect[55] (also known as Stone-Thrower[56]-Wales or STW defect) predominately studied in graphene[34,36,37] and carbon nanotubes.[57] A 7/7 dipole herein is the less analyzed V_2 (55–77) divacancy structure[58,59] as the five-neighbor bubbles are not aligned along the shared edge of the seven-neighbor bubbles. The stability of 7/7 dipoles was dependent on the direction of the constitutive Burgers vectors. 7/7 $\vec{b}_3$ dislocation dipoles are the least stable whereas 7/7 $\vec{b}_1$ dislocation dipoles are the most stable based on the temporal evolution of the dipole orientation (Fig. 14).

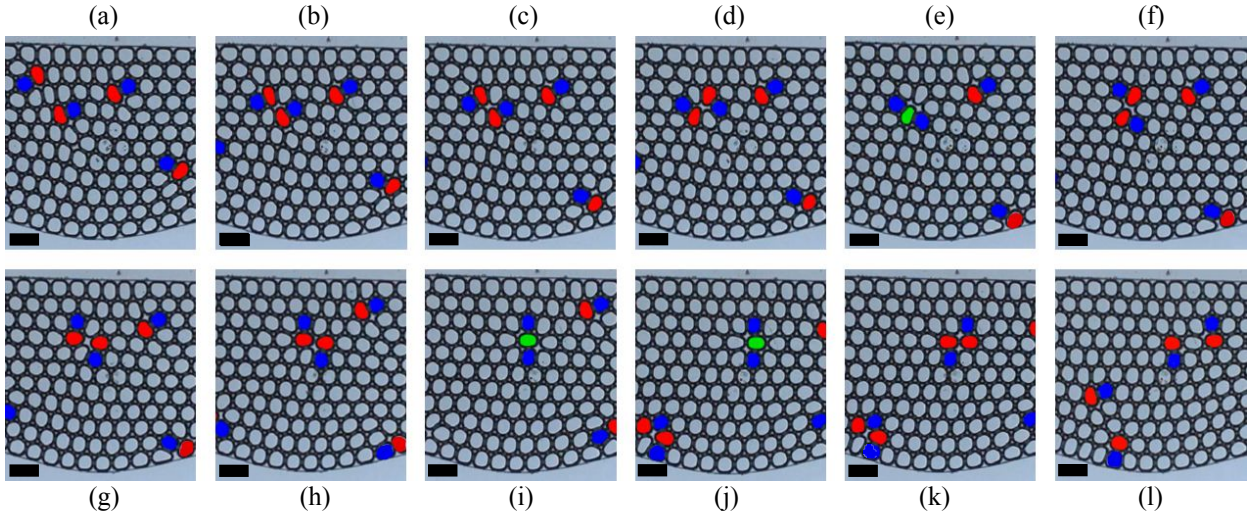

Fig. 14 (a-c) Formation of a 7/7 $\vec{b}_3$ dislocation dipole which (d) temporarily reforms with $\vec{b}_2$ orientation. (d-f) The dislocations comprising the dipole effectively pass through one another [the dipole in (f) has different five-neighbor bubbles than the dipole in (d), switching the respective signs of the dislocations] *via* an intermediate 5/8/5 structure. The dislocations do not undergo separation due to the high packing density of the bubbles. (g-h) A 7/7 $\vec{b}_1$ dislocation dipole develops from the convergence of the seven-neighbor bubbles in the direction of flow. The bubbles of the 7/7 $\vec{b}_1$ dislocation dipole are identical to the initial 7/7 $\vec{b}_3$ dislocation dipole with the number of nearest neighbors inverted. (h-l) The resulting dipole dissociates as the $\vec{b}_1$ dislocations pass through one another and separate. Experimental conditions: 0.75 mL h^{-1}, 450 mbar and $\Phi = 0.96$ with elapsed time of 87.5 ms. Scale bar is 250 μm.

Upon formation of the 7/7 $\vec{b}_3$ dislocation dipole (Fig. 14b), the joint retraction of the seven-neighbor bubbles of each dislocation initiates a different T1 topological rearrangement

(Fig. 14c-d) than dislocation glide or reflection in the bulk (see Fig. 10). A new 7/7 dipole is formed with $\vec{b}_2$ orientation consisting of the same five-neighbor bubbles (Fig. 14d *vs.* Fig. 14b). A single 5/8/5 structure is formed (Fig. 14e) as the bubbles undergoing retraction diverge farther with a calculated[49] strain rate of –65 s^{-1}. A 7/7 $\vec{b}_2$ dislocation dipole is temporarily reformed with the dislocations switching signs (Fig. 14f *vs.* Fig. 14d) as the bubbles aligned with the direction of flow converge in the empty space adjacent to the 5/8/5 structure. These $\vec{b}_2$ dislocations have been observed to glide away from each other under less optimal conditions (i.e. reduced packing density, nearby dislocations along a slip plane, and/or transitioning alignment of the bubble rows from expansion-contraction flow). In graphene, the transformation of a 5/8/5 structure into the V_2 (55–77) structure by bond rotation[58] and the reciprocal process have been elucidated with the V_2 (55–77) structure being less energetically favorable.[59]

A T1 topological rearrangement (driven by the upstream seven-neighbor bubble moving with flow) forms a new 7/7 dipole with $\vec{b}_1$ orientation consisting of the same five-neighbor bubbles (Fig. 14h *vs.* Fig. 14f). Thus, 7/7 $\vec{b}_1$ dislocation dipoles are the most stable, being most aligned with the flow and least aligned with the tensile forces of the expansion. As the straighter row containing the seven-neighbor bubbles accelerates past the row below, a 5/8/5 structure is formed before the dislocations pass through each other and glide in opposite directions (Fig. 14h-l). Rearrangement to the more stable $\vec{b}_1$ configuration before disassociation also occurs when the initial 7/7 dipole has $\vec{b}_2$ orientation. In both cases, the Burgers vector is conserved (remaining zero), but the direction of lattice distortion has changed. Dislocation pass through *via* an intermediate 5/8/5 structure follows the direct formation of a 7/7 $\vec{b}_1$ dislocation dipole.

3.7.2 5/5 dipoles. Also developing from irregular dislocation events, 5/5 dipoles generally formed in the region downstream (Fig. 15) or upstream (Fig. 16) of a contraction with calculated[49] strain rates of 40-50 s^{-1}. 5/5 dipoles resemble the Inverse-Stone-Wales (ISW) defect (or ISTW defect),[60,61] which has a higher formation energy than a SW defect but can develop in graphene under nonequilibrium conditions.[36] The ISW defect, which violates the "isolated pentagon rule" regarding the stability of fullerenes,[62-64] provides a particularly reactive site on graphene.[36] The bubble packing density and the location within the channel determined the temporal evolution of these dipoles. 5/5 dipoles either separated (Fig. 15) or one dislocation passed through the other *via* an intermediate ring structure (Fig. 16).

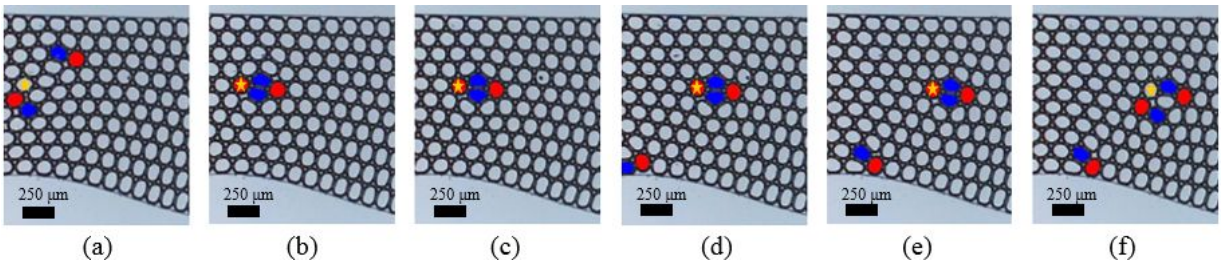

Fig. 15 (a-c) Formation of a 5/5 $\vec{b}_2$ dislocation dipole, (d-e) which is subsequently advected by the foam. Prior to separation the dipole rotates to align with the flowing foam. (f) Once the dipole reaches the expansion region, a T1 topological rearrangement occurs as the (starred) upstream seven-neighbor bubble preferentially diverges along the direction of tension with the bubble in the positive third direction. The dislocations separate and move apart opposite of the original respective gliding directions (elapsed time 40 ms). Experimental conditions: 1 mL h^{-1}, 550 mbar and $\Phi = 0.96$.

The five-neighbor bubbles adopt a semicircular configuration upon formation of the 5/5 dipole, generating a large contact line as the respective surfaces are flattened and extended (Fig. 15c,d). Proximal to the dipole, the adjacent bubbles to the five-neighbor bubbles adopt a similar semicircular configuration consistent with the corresponding distortion of the lattice structure in graphene. An ISW defect modifies the structure of the lattice edges (unlike the SW defect) due to the presence of two extra atoms with respect to the perfect lattice.[65] In fact, the ISW defect is a 16-atom "blister" with a nonzero height above the graphene plane.[60] The deformation required for the bubbles to remain in this configuration is indicative of an energetically unfavorable structure. Once the dipole reaches the expansion region, a T1 topological rearrangement occurs as the (starred) upstream seven-neighbor bubble preferentially diverges along the direction of tension with the semicircular bubble proximal to the dipole (Fig. 15d-f). The dislocations separate and move apart opposite of the original respective gliding directions. Formation of a 5/5 dipole with different orientation than the initial gliding dislocations can occur in the region downstream of a contraction in the model system due to the reduced bubble packing density (ESI† Fig. S4).

Dislocations comprising a 5/5 dipole can pass through each other *via* an intermediate ring structure (Fig. 16). The bottommost five-neighbor bubble of the dipole preferentially converges along the direction of compression with the (green starred) bubble two rows below (Fig. 16b,c). The T1 topological rearrangement forms an intermediate six-membered ring structure (Fig. 16d), comprised of three dislocation pairs around a triangular-shaped central bubble. The hexagonal geometry of perfect packing is vertically stretched, giving the ring structure a kite shape. The central bubble subsequently diverges from the (unstarred) seven-neighbor bubble in the negative third direction, which forms a new 5/5 dipole (Fig. 16e). The calculated[49] strain rates (or shear rates as in ESI† Fig. S4) associated with the shifting of the central bubble with respect to the surrounding five-neighbored bubbles were 30-35 s^{-1}. The dislocations of the reformed 5/5 dipole have the orientation of the initial dipole, but one dislocation has passed through the other as the new dipole contains only two of the initial bubbles (Fig. 16c *vs*. 16e). These dislocations separate and glide away from one another.

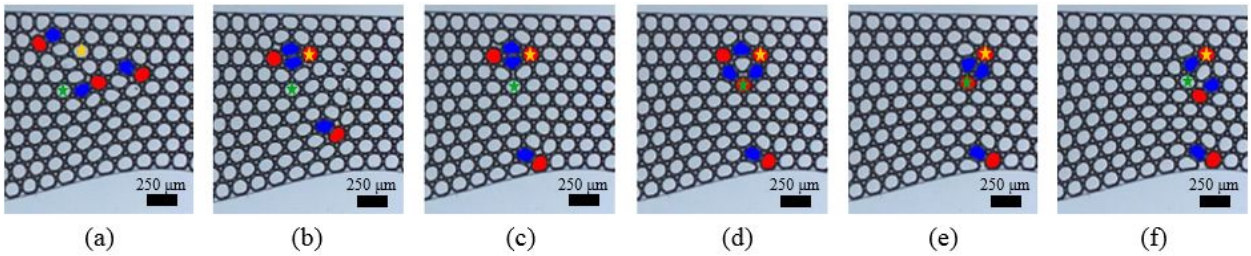

Fig. 16 (a-b) Formation of a 5/5 $\vec{b}_3$ dislocation dipole, (c) which is advected by the foam before the bottommost five-neighbor bubble preferentially converges along the direction of compression with the (green starred) bubble two rows below. (d) An intermediate six-membered ring structure is formed, comprised of three dislocation pairs around a triangular-shaped central bubble. A second T1 topological event transpires as the central bubble diverges from the (unstarred) upstream seven-neighbor bubble and (e) a new 5/5 dipole forms with equivalent orientation (albeit different positioning due to the different alignment of the surrounding crystal). The dislocations have passed through each other [the 5/5 dipole in (e) has the identical bubbles comprising the upstream dislocation, which in (b,c) were formerly part of the downstream dislocation]. (f) These dislocations separate and glide away from one another (elapsed time 30 ms). Experimental conditions: 1 mL h^{-1}, 550 mbar and $\Phi = 0.96$.

Dislocation pass through after formation of a 5/5 dipole was only observed through an intermediate ring structure (analogous to pass through after formation of a 7/7 dipole by means of a 5/8/5 structure). The six-membered ring was first identified for graphene as a 24-atom defect

blister,[60] with three-fold symmetry and a higher formation energy than the ISW defect.[66] Therefore, this partially dissociated ISW defect was not theorized to evolve directly from the ISW defect (as discovered in flowing foam herein), but rather a pathway was proposed to synthesize the ISW defect by first transforming an SW defect into the six-membered ring.[61] In the present work, the largest ring structure was observed under the reduced packing density of the model system at the downstream end of the tension rearrangement zone (Fig. 17a). The eight-membered ring structure is comprised of four dislocation pairs surrounding both five-neighbor bubbles of the initial 5/5 dipole (Fig 17b). Thus, a 5/5 dipole is not reformed and the dislocations that separate under these conditions are composed of entirely different bubbles than the initial dipole (Fig. 17c).

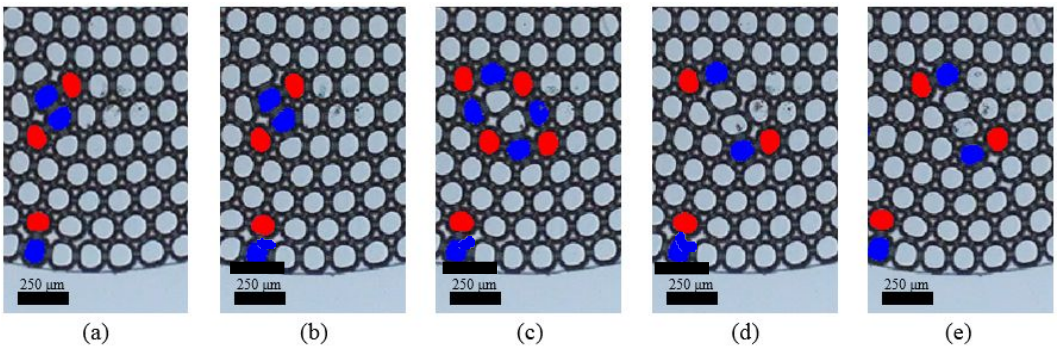

Fig. 17 (a) Formation of a 5/5 $\vec{b}_3$ dislocation dipole in the reduced local packing density at the downstream end of the tension rearrangement zone. (b-c) Two simultaneous T1 topological rearrangements occur as the semi-circular neighbors outside of the dipole diverge while the initial five-neighbored bubbles are forced into close contact. The intermediate eight-membered ring structure bears a striking resemblance to a ring structure formed in graphene during the reconstruction process after damage by irradiation.[35] (c-e) Two simultaneous T1 topological rearrangements occur as each central bubble within the ring converges with a five-neighbored bubble (top bubble in the direction of flow and bottom bubble against the direction of flow). The calculated[49] shear and strain rates associated with the shifting of the central bubbles were $-40 s^{-1}$ and $-50\ s^{-1}$ respectively. Contrary to previous pass through events, the dislocations that separate are composed of entirely different bubbles than the initial dipole (elapsed time 15 ms). Experimental conditions: 1 mL h^{-1}, 500 mbar and $\Phi = 0.94$. Scale bar is 250 μm.

4 Conclusions

By subjecting densely packed wet foam to expansion-contraction flow, dislocations were found to cyclically reflect in tension or compression within two independent rearrangement zones of the monodisperse bubble matrix. The mechanisms of reflection under tension were expanded as dislocations can reflect "at the wall" without penetrating the wall bubble row by either a "dislocation-union" or a "dislocation-split" reflection. Hopping[14] (arising from the reduced packing density of bubbles at the wall) was established as a form of dislocation reflection in an expansion, which shifts the reflected dislocation against flow to the adjacent slip plane. Homogeneous dislocation nucleation was observed in isolated regions of the channel. The nucleated dislocation either acted as a source to replace a dislocation that does not reflect into the compression rearrangement zone or as a reactant that changes the direction of a gliding dislocation upon collision.

The use of an asymmetric channel created a dichotomy in the model crystalline system between straighter, aligned bubble rows near the horizontal wall and curved, misaligned rows near the sinusoidal wall due to the corresponding streamlines within the channel. Dislocation glide

away from the sinusoidal wall misaligns the crystal structure and glide away from the horizontal wall realigns the bubble rows. Localized dislocations gliding into the aligned rows of the crystal moved by stick-slip motion in the contraction region and could undergo premature dislocation reflection in the bulk of the foam in the expansion region.

7/7 dipoles were found to rearrange to a more stable configuration aligned with the foam flow through directional changes in the constitutive Burgers vectors before disassociating. The dislocations pass through each other *via* an intermediate 5/8/5 structure and glide away from one another. For all experimental conditions studied, dislocations comprising 7/7 dipoles were unable to pass through each other in the expansion region along the direction of tension. 5/5 dipoles resemble the Inverse-Stone-Wales defect in graphene[60,61] with the five-neighbor bubbles of the tightly coupled dislocations adopting semicircular configurations. The dislocations of the 5/5 dipole were discovered to only pass through each other *via* intermediate ring structures. The most common ring structure consisted of three dislocation pairs around a triangular central bubble, resembling the partially dissociated ISW defect in graphene.[61,66]

Bubbles and foams have a long record of being employed as model crystalline systems, and the present work utilizes microfluidics for expanded visualization and analysis of crystalline deformation. The ability to tune the foam properties enabled the selection of a suitable model system as well as the capacity to study how gas area fraction impacts the crystalline behavior of the system. Historically, the majority of foam research focused on the static properties of dry foams,[67] creating a continued need for work on the rheology of wet foams (and emulsions).[14-19,21-26,42,51,54,68-77] The simple channel design for generating expansion-contraction flow shapes the flowing crystal with varying degrees of alignment. The impact of the gradient in alignment on dislocation glide, reflection, and nucleation cannot be studied from commonly used symmetric designs. The relationship between 5/5 dipoles and intermediate ring structures may shed light on a method of precise synthesis of the ISW defect, which promotes a favorable increase in the reactivity of graphene.[36] Future microfluidic work could make use of a wedge-shaped channel[72,78] to attempt the creation of multiple independent tension rearrangement zones. An extended expansion region to force the flowing crystal out of long-range order to study 2-D phase transitions,[79] specifically melting into an expansion region and recrystallization into a contraction region, could be another promising area of research.

Acknowledgements

This work was funded in part by the National Science Foundation under Grant No. CBET-17055703.

References

1. L. Bragg and J. F. Nye, *Proc. R. Soc. London, Ser. A*, 1947, **190**, 474–481.
2. A. S. Argon and H. Y. Kuo, *Mater. Sci. Eng.*, 1979, **39**, 101–109.
3. M. J. Bowick, L. Giomi, H. Shin and C. K. Thomas, *Phys. Rev. E: Stat., Nonlinear, Soft Matter Phys.*, 2008, **77**, 021602.
4. A. van der Net, W. Drenckhan, D. Weaire and S. Hutzler, *Soft Matter*, 2006, **2**, 129–134.
5. M. Vignes-Adler and D. Weaire, *Curr. Opin. Colloid Interface Sci.*, 2009, **13**, 141–149.
6. W. Drenckhan and D. Langevin, *Curr. Opin. Colloid Interface Sci.*, 2010, **15**, 341–358.
7. A. M. Gañán-Calvo and J. M. Gordillo, *Phys. Rev. Lett.*, 2001, **87**, 274501.
8. C. S. Smith, *J. Appl. Phys.*, 1949, **20**, 631.
9. E. Kumacheva, P. Garstecki, H. Wu and G. M. Whitesides, *Phys. Rev. Lett.*, 2003, **91**, 128301.
10. P. Garstecki and G. M. Whitesides, *Phys. Rev. Lett.*, 2006, **97**, 24503.
11. M. Hashimoto, B. Mayers, P. Garstecki and G. M. Whitesides, *Small*, 2006, **2**, 1292–1298.
12. A. van der Net, G. W. Delaney, W. Drenckhan, D. Weaire and S. Hutzler, *Colloids Surf., A*, 2007, **309**, 117–124.
13. A. van der Net, A. Gryson, M. Ranft, F. Elias, C. Stubenrauch and W. Drenckhan, *Colloids Surf., A*, 2009, **346**, 5–10.
14. M. E. Rosa and M. A. Fortes, *Philos. Mag. A*, 1998, **77**, 1423–1446.
15. E. Fukushima and A. Ookawa, *J. Phys. Soc. Jpn.*, 1953, **8**, 609–614.
16. M. Arciniaga, C.-C. Kuo and M. Dennin, *Colloids Surf., A*, 2011 **382**, 36–41.
17. C.-C. Kuo and M. Dennin, *J. Rheol.*, 2012, **56**, 527–541.
18. A. Gouldstone, K. J. van Vliet and S. Suresh, *Nature*, 2001, **411**, 656.
19. K. J. van Vliet and S. Suresh, *Philos. Mag. A*, 2002, **82**, 1993–2001.
20. B. Dollet and C. Bocher, *Eur. Phys. J. E*, 2015, **38**, 123.
21. D. Chen, K. W. Desmond and E. R. Weeks, *Soft Matter*, 2012, **8**, 10486–10492.
22. D. Chen, K. W. Desmond and E. R. Weeks, *Phys. Rev. E: Stat., Nonlinear, Soft Matter Phys.*, 2015, **91**, 062306.
23. Z. Jing, S. Wang, M. Lv, Z. Wang and X. Luo, *Soft Matter*, 2015, **11**, 2973–2982.
24. Y. Wang, K. Krishan and M. Dennin, *Phys. Rev. E: Stat., Nonlinear, Soft Matter Phys.*, 2006, **73**, 031401.
25. Z. Jing, S. Wang, M. Lv, Z. Wang and X. Luo, *J. Fluids Eng.*, 2015, **137**, 041206.
26. Y. Gai, C. M. Leong, W. Cai and S. K. Y. Tang, *PNAS*, 2016, **113,** 12082–12087.
27. J. Yan, S. C. Bae, and S. Granick, *Soft Matter*, 2014, **11**, 147–153.
28. A. R. Bausch, M. J. Bowick, A. Cacciuto, A. D. Dinsmore, M. F. Hsu, D. R. Nelson, et al., *Science*, 2003, **299**, 1716–1718.
29. T. Einert, P. Lipowsky, J. Schilling, M. J. Bowick and A. R. Bausch, *Langmuir*, 2005 ,21, 12076–12079.
30. P. Lipowsky, M. J. Bowick, J. H. Meinke, D. R. Nelson and A. R. Bausch, *Nat. Mater.*, 2005, **4**, 407–411.
31. W. T. M. Irvine, A. D. Hollingsworth, D. G. Grier and P. M. Chaikin, *PNAS*, 2013, **110**, 15544–15548.
32. D. A. Beller and D. R. Nelson, *Phys. Rev. E: Stat., Nonlinear, Soft Matter Phys.*, 2016, **94**, 033004.

33. C. Gómez-Navarro, J. C. Meyer, R. S. Sundaram, A. Chuvilin, S. Kurasch, M. Burghard, K. Kern and U. Kaiser, *Nano Lett.*, 2010, **10**, 1144–1148.
34. J. C. Meyer, C. Kisielowski, R. Erni, M. D. Rossell, M. F. Crommie and A. Zettl, *Nano Lett.*, 2008, **8**, 3582–3586.
35. G.-D. Lee, E. Yoon, K. He, A. W. Robertson and J. H. Warner, *Nanoscale*, 2014, **6**, 14836–14844,
36. F. Banhart, J. Kotakoski and A. V. Krasheninnikov, *ACS Nano*, 2011, **5**, 26–41.
37. S. T. Skowron, I. V. Lebedeva, A. M. Popov and E. Bichoutskaia, *Chem. Soc. Rev.*, 2015, **44**, 3143–3176.
38. S. Balendhran, S. Walia, H. Nili, S. Sriram and M. Bhaskaran, *Small*, 2015, **11**, 640–652.
39. D. C. Duffy, J. C. McDonald, O. J. A. Schueller and G. M. Whitesides, *Anal. Chem.*, 1998, **70**, 4974–4984.
40. C. A. Conn, K. Ma, G. J. Hirasaki and S. L. Biswal, *Lab Chip*, 2014, **14**, 3968–3977.
41. D. Vecchiolla, V. Giri and S. L. Biswal, *Soft Matter*, 2018, **14**, 9312–9325.
42. Y. Bertho, C. Becco and N. Vandewalle, *Phys. Rev. E: Stat., Nonlinear, Soft Matter Phys.*, 2006, **73**, 056309.
43. B. Dollet, *J. Rheol.*, 2010, **54**, 741–760.
44. S. A. Jones, B. Dollet, N. Slosse, Y. Jiang, S. J. Cox and F. Graner, *Colloids Surf., A*, 2011, **382**, 18–23.
45. M. R. Stukan, E. S. Boek, J. T. Padding, W. J. Briels and J. P. Crawshaw, *Soft Matter*, 2008, **4**, 870–879.
46. J. Zhang, M. Li, W. H. Li and G. Alici. *J. Micromech. Microeng.*, 2013, **23**, 085023.
47. S. Park, Y. S. Huh, H. G. Craighead and D. Erickson, *PNAS*, 2009, **106**, 15549–15554.
48. E. J. Stamhuis, *Aquat. Ecol.*, 2006, **40**, 463–479.
49. W. Thielicke and E. J. Stamhuis, *J. Open Res. Software*, 2014, **2**, e30.
50. W. Thielicke, "The flapping flight of birds: Analysis and application," [S.l.]: [S.n.], 2014.
51. Y. Gai, A. Bick and S. K. Y. Tang, *Phys. Rev. Fluids*, 2019, **4**, 014201.
52. C. M. Leong, Y. Gai and S. K. Y. Tang, *Phys. Fluids*, 2018, **30**, 032002.
53. F. R. N. Nabarro, *Theory of crystal dislocations*. Dover Publications, New York, 1987.
54. S. Tewari, D. Schiemann, D. J. Durian, C. M. Knobler, S. A. Langer and A. J. Liu, *Phys. Rev. E: Stat. Phys., Plasmas, Fluids, Relat. Interdiscip. Top.*, 1999, **60**, 4385–4396.
55. A. J. Stone and D. J. Wales, *Chem. Phys. Lett.*, 1986, **128**, 501–503.
56. R. A. Thrower, *Chem. Phys. Carbon*, 1969, **5**, 217–319.
57. M. Buongiorno Nardelli, B. I. Yakobson and J. Bernholc, *Phys. Rev. B*, 1998, **57**, R4277–R4280.
58. J. Kotakoski, A. V. Krasheninnikov, U. Kaiser and J. C. Meyer, *Phys. Rev. Lett.*, 2011, **106**, 105505.
59. Z. Wang, Y. G. Zhou, J. Bang, M. P. Prange, S. B. Zhang and F. Gao, *J. Phys. Chem. C*, 2012, **116**, 16070–16079.
60. M. T. Lusk and L. D. Carr, *Phys. Rev. Lett.*, 2008, **100**, 175503.
61. M. T. Lusk, D. T. Wu and L. D. Carr, *Phys. Rev. B: Condens. Matter Mater. Phys.*, 2010, **81**, 155444.
62. H. W. Kroto, *Nature*, 1987, **329**, 529–531.

63. T. G. Schmalz, W. A. Seitz, D. J. Klein and G. E. Hite, *J. Am. Chem. Soc.*, 1988, **110**, 1113–1127.
64. Y.-Z. Tan, S.-Y. Xie, R.-B. Huang and L.-S. Zheng, *Nat. Chem.*, 2009, **1**, 450–460.
65. A. Carpio, L. L. Bonilla, F. de Juan and M. A. H. Vozmediano, *New J. Phys*., 2008, **10**, 053021.
66. M. T. Lusk and L. D. Carr, *Carbon*, 2009, **47**, 2226–2232.
67. D. L. Weaire and S. Hutzler, *The physics of foams*. Clarendon Press, Oxford University Press, Oxford, 2001.
68. G. Debrégeas, H. Tabuteau and J.-M. di Meglio, *Phys. Rev. Lett.*, 2001, **87**, 178305.
69. J. Lauridsen, M. Twardos and M. Dennin, *Phys. Rev. Lett.*, 2002, **89**, 098303.
70. A. D. Gopal and D. J. Durian, *Phys. Rev. Lett.*, 2003, **91**, 188303.
71. M. Dennin, *Phys. Rev. E: Stat., Nonlinear, Soft Matter Phys.*, 2004, **70**, 041406.
72. W. Drenckhan, S. J. Cox, G. Delaney, H. Holste, D. Weaire and N. Kern, *Colloids Surf., A*, 2005, **263**, 52–64.
73. B. Dollet and F. Graner, *J. Fluid Mech.*, 2007, **585**, 181–211.
74. R. Lespiat, S. Cohen-Addad and R. Höhler, *Phys. Rev. Lett.*, 2011, **106**, 148302.
75. K. W. Desmond, P. J. Young, D. Chen and E. R. Weeks, *Soft Matter*, 2013, **9**, 3424–3436.
76. G. Katgert, B. P. Tighe and M. van Hecke, *Soft Matter*, 2013, **9**, 9739–9746.
77. S. Cohen-Addad, R. Höhler and O. Pitois, *Annu. Rev. Fluid Mech.*, 2013, **45**, 241–267.
78. E. Surenjav, C. Priest, S. Herminghaus and R. Seemann, *Lab Chip*, 2009, **9,** 325–330.
79. U. Gasser, *J. Phys.: Condens*. *Matter*, 2009, **21**, 203101.

TABLE OF CONTENTS

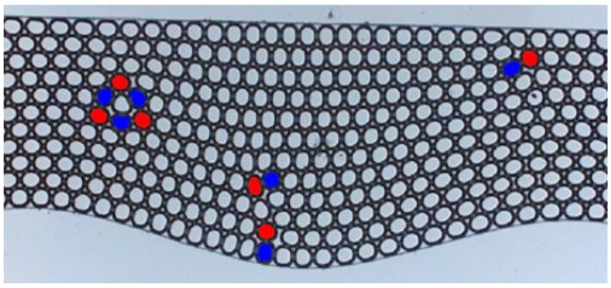

Dislocation glide, reflection, nucleation, and dipole transformations from extensional and compressive stresses within monodisperse wet foam subjected to expansion-contraction flow.